Possible influence of Sudden Stratospheric Warmings on the atmospheric environment in the Beijing-Tianjin-Hebei region

Qian Lu[1, 2, 3] , Jian Rao[1, *], Chunhua Shi[1], Dong Guo[1], Guiqin Fu[2], Ji Wang[4], Zhuoqi Liang[1]

[1]Key Laboratory of Meteorological Disaster, Ministry of Education (KLME) / Joint International Research Laboratory of Climate and Environment Change (ILCEC) / Collaborative Innovation Center on Forecast and Evaluation of Meteorological Disasters (CIC-FEMD), Nanjing University of Information Science and Technology, Nanjing 210044, China
[2]Key Laboratory of Meteorology and Ecological Environment of Hebei Province, Shijiazhuang 050021, China
[3]Chengde Meteorological Service of Hebei Province, Chengde, Hebei 067000, China
[4]Beijing Regional Climate Center, Beijing 100089, China

Correspondence to: Jian Rao (raojian@nuist.edu.cn)

Abstract. Using the ERA5 and MERRA2 reanalysis, and surface meteorological observation data, this study explores the possible impact of the sudden stratospheric warming (SSW) events on air quality in the Beijing-Tianjin-Hebei (BTH) region. As the duration of split SSW events is longer and the stratospheric signal pulses propagate further downward than displacement SSWs, subseasonal variability of the atmospheric particulates in the BTH is larger during split SSWs. The air particulate concentration is light before the SSW onset due to the enhanced perturbation in the troposphere associated with strengthened planetary waves. The air particulate concentration around the SSW onset dates begins to rise due to weakening of the tropospheric disturbance as the enhanced planetary waves enter the stratosphere. In the decaying period of the SSW, the air particulate concentration decreases as the stratospheric negative Northern Annular Mode (NAM) signal propagates downward. Specifically, in the pre-SSW period of displacement (split) SSW events, a wavenumber-1-like (wavenumber-2-like) anomaly pattern is strengthened. The East Asian winter monsoon intensifies as the east Asian trough is deepened especially before the split SSW event onset, leading to a cleaning period. Around the SSW onset period as the tropospheric perturbation diminishes and the East Asian winter monsoon weakens, a surge of air particulate concentration is observed. After the SSW onset, due to the downward propagation of the stratospheric negative NAM signal, cold anomalies form in the northeastern East Asia especially for split SSWs, corresponding to a cleaning period in the BHT region. The local meteorological conditions during the SSWs are also discussed.

Key words: Sudden stratospheric warming (SSW), Beijing-Tianjin-Hebei (BTH), Atmospheric environment, East Asian winter monsoon

1. Introduction

Haze pollution is reported to cause serious adverse effects on the ecological environment, daily life and transportation, damage the health of humans and animals, and even reduce the yield of crops (Hu et al., 2015; Chen et al., 2020; Bu et al., 2021). Considering the wide influence of the atmospheric particulate, haze has become a hot topic attracting widespread

concern, although the air quality has improved in the past decade (Ding et al., 2019; Li et al., 2019). The source analysis of pollutants shows that the primary local emission from factories and automobiles, atmospheric transport from surrounding regions, and secondary formation of aerosols by chemistry reactions produce the main atmospheric haze pollution (Huang et

35 al., 2015; Zhao et al., 2019). Adverse meteorological conditions can lead to fast accumulation or slow dilution and difficult diffusion of pollutants in the atmosphere, which are also the background condition of heavy pollution weather (Li et al., 2018; Dang and Liao, 2019; Chang et al., 2020). Dormancy of the east Asian winter monsoon and the rise of winter temperature are possibly accountable for changes of haze days across North China (Yin et al., 2015; Li et al., 2016). On the hemispheric scale, the wintertime heavy haze in parts of North China often occurs when the Arctic Oscillation (AO) is in the positive

40 phase (Li et al., 2018; Yin et al., 2017). As the key system of haze pollution in North China, at times an anomalous anticyclone developed in the Bohai Sea, which is usually accompanied by air quality decline (Wu et al., 2017). The large-scale atmospheric circulation and meteorological conditions provide a background for the occurrence and decay of heavy haze days (Wang and Chen, 2016; Li et al., 2018). For example, certain conditions are not conducive to the dilution and diffusion of air pollutants, such as the reduction of the local boundary layer height, increase in the static stability (or even

45 development of inversion layer), and deceleration of the near surface wind speed (Huang et al., 2018, 2020; Yang et al., 2016). With those conditions, higher relative humidity might promote the moisture absorption and growth for air particulates (Feng et al., 2018).

Sudden stratospheric warming (SSW) is a rapid and violent warming phenomenon in the polar stratosphere in winter (Charlton and Polvani, 2007; Butler et al., 2015; Rao et al., 2018; Lu et al., 2021). When an SSW occurs, the atmospheric

50 temperature in the polar cap region of the stratosphere suddenly rises, which can increase by tens of degrees Celsius within a week (Charlton and Polvani, 2007; Rao and Garfinkel, 2020; Lu et al., 2021). After the SSW onset, the stratospheric anomalies can propagate downward, and the tropospheric circulation is adjusted accordingly (Baldwin et al., 2001; Rao et al., 2021). If the meridional gradient of the temperature between 60 and 90°N reverses, and the circumpolar westerly winds at 10 hPa and 60°N are significantly weakened but do not reverse to the easterly winds, the SSW is usually classified as a minor

55 event. If the circumpolar westerly winds reverse to the easterly winds at 10 hPa and 60°N, it is called a major SSW (Charlton and Polvani, 2007; Rao et al., 2018; Butler et al., 2020; Baldwin et al., 2021). According to the morphology of the polar vortex shape around the onset time, major SSWs can be further categorized as polar vortex displacement SSW events and polar vortex split SSW events (Charlton and Polvani, 2007; Baldwin et al., 2021). Vortex displacement SSWs are associated with enhanced planetary wavenumber 1, while vortex split SSWs are alternatively forced by wavenumber 1 and

60 wavenumber 2 (Karpechko et al., 2018; Liu et al., 2019; Rao et al., 2019a, 2020; Baldwin et al., 2021). On average, six or seven SSW events occur in a decade, and it can appear in months from November to March, with the most concentrated from January to February (Cao et al., 2019; Liu et al., 2019; Rao and Garfinkel, 2021). The SSW appear unevenly in every decade and exhibits a significant interdecadal variation (Rao et al., 2021). SSW event is a typical phenomenon of two-way coupling between stratosphere and troposphere (Hu et al., 2014). Before the SSWs onset, the upward propagation of

65 planetary waves from the troposphere to the stratosphere is enhanced (De La Cámara et al., 2019; Rao et al., 2019b), which

might be owing to the preceding tropospheric blocking and/or deepening of the climatological trough (Rao et al., 2018, 2020; Baldwin et al., 2021). After the SSWs onset, the atmospheric circulation anomalies generated by SSW events in the stratosphere can propagate downward to the troposphere and affect the weather and climate in the troposphere (Lu et al., 2021b; Baldwin et al., 2021). The weakened stratospheric polar vortex during SSW events is mainly projected onto the

70 negative phase of the northern annular mode (NAM). With the negative NAM signal descending to lower levels, the tropospheric anomaly circulation evolves into a pattern resembling the negative phase of the Arctic Oscillation (AO) or the negative phase of the North Atlantic Oscillation (NAO) in the Atlantic sector (Baldwin and Dunkerton, 1999, 2001). On the probabilistic sense, cold air outbreak is likely to increase on the northern continents (Yu et al., 2015; Lu et al., 2021b; Rao et al., 2021). Although most previous studies emphasized the possible impact of the stratospheric disturbance on the

75 tropospheric circulation, the possible linkage between the stratospheric anomalies and the subseasonal variability of the regional air quality is still not well explored.

Existing evidence mainly focuses on the possible impact of tropospheric climate anomalies and the wave train like teleconnections on the regional air pollutions, but few studies investigate the possible impact of stratospheric changes on regional haze pollution. Given that the tropospheric climate anomalies can be affected by the stratospheric changes, the haze

80 pollution in the Beijing-Tianjin-Hebei (BTH) region associated with atmospheric circulation variability may also be affected by the stratospheric changes (Chang et al., 2020; Huang et al., 2021; Lu et al., 2021a, 2022). A recent study reports that the weakening of stratospheric polar vortex in the winter of 2015/16 can lead to easier diffusion of pollutants and a gradual improvement of the air quality in the BTH region (Huang et al., 2021). Comparing the three SSW events in February 2018, January 2019 and January 2021, it is shown that the subseasonal variability of the $PM_{2.5}$ concentration in the BTH region

85 might be enhanced after the stratospheric anomalies propagate downward to the troposphere and near surface (Lu et al., 2021a, 2022). However, the generalization of the possible impact of the SSWs on the BHT region in previous studies should be verified using abundant historical SSW samples. This study will adopt more SSW samples and robustly establish the relationship between the SSW and the air particulate concentration in the BHT region. Hitherto, we still do not clearly know yet if the vortex displacement and split SSWs have similar or different impacts on the regional atmospheric environment in

90 the BTH region.

The paper is constructed as follows. Following this part, the data and methodology are briefly described in section 2. Section 3 shows the composite of the zonal-mean circulation anomalies for displacement SSW events and split SSW events. Evolutions of large-scale circulation anomalies accounting for the subseasonal variability of the atmospheric particulates in the BHT region during different periods of the two types of SSWs are analyzed in section 4. Section 5 analyzes the local

95 meteorological anomalies in the BTH region during different periods of the two types of SSWs. Section 6 display the composite atmospheric environment quality in the BTH region using different metrics during the two types of SSWs. Finally, section 7 presents summary and discussion.

2. Data and methodology

Daily reanalysis data from 1980 to 2021 is provided by the European Center for Medium Range Weather Forecasts, and its
fifth-generation reanalysis is used (ERA5) (Hersbach et al., 2020). The atmospheric data used in this study include the
geopotential height (Z, geopotential divided by 9.8), the zonal wind (U), the meridional wind (V) and air temperature (T).
This reanalysis was downloaded at a $1° \times 1°$ horizontal resolution at 37 pressure levels spanning from 1000 hPa to 1 hPa.
The ERA5 surface data employed in this study include the sea level pressure (SLP), surface air temperate (SAT) and
planetary boundary layer height (PBLH), which is also collected at a $1° \times 1°$ horizontal resolution. The daily observation
data of minimum visibility, haze, fog and light fog in the cities of Beijing, Tianjin and Shijiazhuang are provided by the
China Meteorological Information Center. The second Modern-Era Retrospective analysis for Research and Applications
(MERRA-2) is also used, which has a horizontal resolution of $0.625° \times 0.5°$ (longitude $\times$ latitude). The MERRA2 reanalysis is
provided by the NASA and begins from 1980 (Gelaro et al., 2017). The aerosol optical depth (AOD) data from the
MERRA2 are used to denote the historical atmospheric environment conditions in the BTH region when the PM$_{2.5}$
concentration was still not a standard observation variable in China. The long-term mean from 1980–2021 on each calendar
day of the year is calculated to denote the raw daily climatology. Daily anomalies refer to the department from this smoothed
daily climatology with a window of 121 days to remove the high-frequency variability.

The modified World Meteorological Organization (WMO) SSW identification algorithm is used to select major SSW
samples and their onset date. When the circumpolar westerly winds at 60°N and 10 hPa reverse to easterly wind and last for
at least 5 days (removing some marginal SSWs), an SSW sample is determined. The first day on which the zonal mean zonal
winds reverse is defined as the SSW onset date. According to the position and shape of polar vortex, major SSW events can
be further divided into two types, polar vortex displacement type and polar vortex split type (Charlton and Polvani, 2007;
Butler et al., 2015; Rao et al., 2021). Vortex-centric diagnostics are used to categorize the type of SSW events (Seviour et al.,
2016). In addition to the vortex-centric parameters, several other metrics can also be calculated based on the two-
dimensional vortex moment diagnosis of the polar vortex geometry. Parameters such as centroid and aspect ratio are used in
order to define a vortex uniquely, and an "equivalent ellipse" is defined as the representative of a vortex(Mitchell et al.,
2011; Seviour et al., 2016). For a simplified purpose, the geopotential height is used to determine the absolute vortex
moments (M_{ab}) and the relative vortex moments (J_{ab}), although similar procedures can also be applied to the Ertel's potential
vorticity. The geopotential height is projected onto a Cartesian coordinate first, and the Arctic polar stereographic projection
is used. Based on this vortex moment diagnosis, several parameters of the stratospheric polar vortex at 10 hPa are finally
determined, including the vortex centroid x-coordinate value, the vortex centroid y-coordinate value, the vortex area in the
Cartesian coordinate, and the aspect ratio between the major and minor axes of the equivalent ellipse (Matthewman et al.,
2009). Finally, the coordinates of the vortex centroid are conversed to the spheric coordinate, and the latitude and longitude
of the vortex centroid are obtained. With the evolution of those metrics during the SSW, a split SSW should meet the
requirement that the aspect ratio is larger than 2.4 for at least seven days during the period from 10 days before to 10 days

after the SSW onset date. A displacement SSW can be confirmed if the vortex centroid latitude is in the equatorward side of a latitude threshold (i.e., 66° N) for at least seven days. Several recent studies reported that this methods can select similar SSW samples as the classification using conventional methods (Seviour et al., 2016; Cao et al., 2019; Rao et al., 2021).

3. Evolutions of the zonal mean circulation anomalies during two types of SSWs

135 According to the WMO algorithms, 17 major SSW events occurred in the Arctic stratosphere during 1981–2021. Some marginal SSWs with a small deceleration of the zonal winds or with one or two days of easterlies have been removed from our composite with a requirement of wind reversals for at least five days. There are 8 vortex displacement SSW events: 24 January 1987, 15 December 1998, 31 December 2001, 5 January 2004, 21 January 2006, 24 February 2007, 22 February 2008, 2 January 2019, and 5 January 2021. There are 9 vortex split SSW events: 2 January 1985, 10 December 1987, 24

140 February 1989, 12 February 2001, 27 January 2009, 12 February 2010, 10 January 2013 11 February 2018 and 2 January 2019. Using the vortex-centric diagnostics and removing the marginal events, it can be found that the vortex displacement SSWs and vortex split SSWs in midwinter is comparable in their numbers during 1980–near present.

The composite pressure-time evolution of the polar cap (i.e., area-averaged over 60–90°N) temperature anomalies, zonal-mean zonal wind anomalies at 60 °N, and polar cap height anomalies from day -20 to day 50 relative to the onset date of the

145 two types of SSWs are shown in Fig. 1. Based on the composite analysis of the zonal mean zonal wind anomalies at 60 °N for all SSW events, the easterly anomalies begin to appear 15 days before the onset dates (Fig. 1d). The significant easterly anomalies in the stratosphere can last until day 40 after the onset of SSWs, and reach the maximum easterly anomaly (-30 m/s) around the onset of SSWs. Since day 20, the easterly anomalies propagate downward to the troposphere. When only displacement SSWs are considered, the zonal mean zonal wind anomalies at 60 °N are relatively weak (Fig. 1e). The easterly

150 wind anomalies begin to appear since day -10 and also maximize around the SSW onset. Overall, the easterly anomalies remain until day 35 days, but significant wind anomalies only appear above 200 hPa and do not propagate downward to lower troposphere. In contrast, the easterly anomalies begin to appear since day -15, and the wind anomaly magnitude is also stronger, reaching the maximum intensity (-35 m/s) several days before the SSW onset. The easterly anomaly signal can last until day 50, which propagate downward to the near surface since day 20. A comparative analysis of the zonal mean zonal

155 wind anomalies for the displacement and split SSWs, it is revealed that the easterly anomalies for split SSWs lasts longer with the anomaly magnitude for the former larger than the latter. The easterly anomalies propagate more downward to the troposphere during the split SSWs than displacement SSWs. The composite results are consistent with the case studies: the circulation anomalies during the February 2018 SSW are more easily propagate downward to the troposphere than the January 2019 SSW (Rao et al., 2020; Lu et al., 2021).

160 According to the principle of thermal winds, the weakening of the 60°N zonal westerly wind is dynamically associated with the decrease and even reversal of the meridional temperature gradient between midlatitudes and the North Pole. The positive temperature anomalies begin to appear since day -20 and reach the maximum value of 15°C on day -8, implying a sudden

rise of the Arctic stratospheric temperature (Fig. 1a). After the onset of SSWs, warm anomalies weaken rapidly and mainly

develop in the stratosphere. Stratospheric warm anomalies can last until day 30 for the composite of all SSW events. When

165 only displacement SSWs are considered, warm anomalies begin to form earlier and appear since day -23 (Fig. 1b). Warm

anomalies persist until day 30 and the warmest anomalies (~20℃) appear on day 5. The warm anomalies do not show a

significant downward propagation and mainly develop above 200 hPa. Similarly, the positive temperature anomalies begin

to appear since day -20 for the split SSWs and reach the maximum value of 15℃ on day -8 (Fig. 1c). Warm anomalies

diminish gradually in the stratosphere and persisted until day 30. No significant zonal-mean temperature anomalies are

170 observed in the troposphere, which might be due to the nonuniform response of the temperature anomalies in the troposphere

and the interlocking distribution of warm and cold anomalies at the same latitudes.
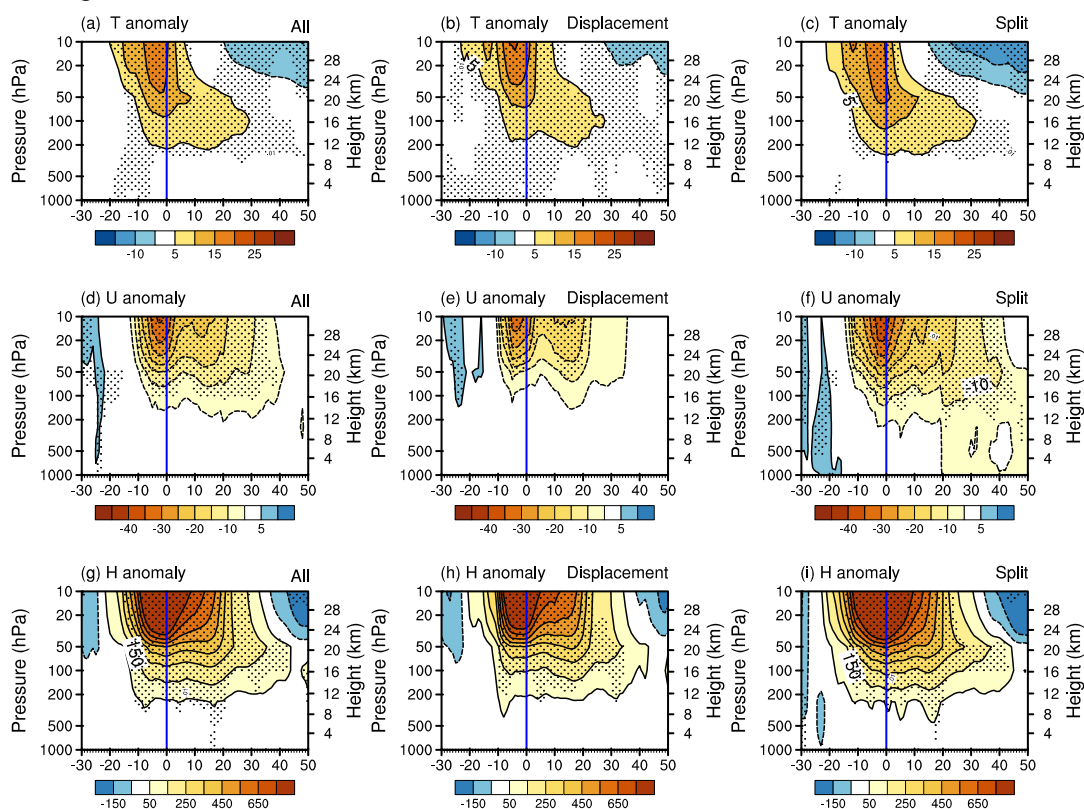
Figure 1: Composite pressure-temporal evolution of the SSW from day -20 to day 50 relative to the onset date for all SSW events (leftmost column), vortex displacement SSWs (middle column) and vortex split SSWs (rightmost column). (a-c) Temperature
175 **anomalies over the polar cap from 60°-90°N (interval: 5; units: ℃). (d-f) Zonal-mean zonal winds at 60°N (interval: 5; units: m s-1). (g-i) Geopotential height anomalies over the polar cap from 60°–90°N (interval: 200; units: gpm). The onset date of the SSW is marked by a vertical blue line. Black dots indicate the composite anomalies at the 95% confidence level using the *t*-test.**

The zonal-mean circulation response to SSWs is also shown for the polar cap heights. According to the principle of

geostrophic winds, accelerated (decelerated) westerly jets in the circumpolar region are accompanied with decrease (rise) of

180 polar cap height and/or the rise (reduce) of the midlatitude heights. Positive geopotential height anomalies denote

development of the negative stratospheric NAM during SSWs (Fig. 1g–i). The positive geopotential height anomalies begin to appear since day -21 and reach the maximum (~750 gpm) on day -10 for the composite of all SSWs. The negative NAM response gradually weakens after the SSWs onset and persists until day 45, and meanwhile the positive height anomalies propagate downward. The negative NAM-like signal can descend to the lowest levels between 200 hPa and 500 hPa since day -10 (Fig. 1g). For displacement SSW events, the positive geopotential height anomalies also begin to appear around day -20 and reach the maximum on day -8 at 10 hPa. After the onset of SSWs, the positive geopotential anomalies gradually weaken and can last until day 45. The positive height anomalies mainly developed in the stratosphere, and the downward propagation is not evident (Fig. 1h). In contrast, the positive geopotential height anomalies appear since day -22 and propagate downward to the troposphere instantly. The maximum positive height response appears on day -12 at 10 hPa (~850 gpm), and afterward the height anomaly magnitude gradually weakens with significant anomalies lasting until day 45 (Fig. 1i). The stratospheric positive geopotential height anomalies can propagate to the troposphere since day 18. In short, the composite of different variables seems to denote that the intensity of the vortex split SSW events is on average stronger than vortex displacement SSWs.

The stratospheric circulation changes drastically during the SSW, which in turn might have a downward influence on the tropospheric circulation. By exploring the tropospheric circulation variability associated with the two types of SSWs, the role of the stratosphere in modulating the regional air environment might be better understood.

4. Large scale circulation anomalies in the stratosphere and troposphere

4.1. Evolution of stratospheric circulation anomalies

SSW is a typical representative of the stratosphere-troposphere coupling in the extratropics, which is followed by discernable tropospheric circulation anomalies (Lu et al., 2021a, 2022). The large circulation anomalies in the stratosphere and troposphere might affect the local meteorological conditions for air particulate diffusion in the BTH region. Figure 2 shows the evolution of 10 hPa geopotential height anomalies in the Northern Hemisphere during vortex displacement and split SSW events. In the pre-SSW period (P1) the geopotential height anomalies distribute as a wavenumber-1-like pattern, and the negative height center is located around the Nova Zembla, and the positive height center is located around the Bering Strait and North Pacific (Fig. 2a). Around the onset date of displacement SSWs and afterward (P2), the polar vortex weakens rapidly. Meanwhile, the North Pole is occupied by large positive height anomalies, and the maximum height anomaly exceeds 800 gpm. The mid-to-low latitudes are covered by weak negative height anomalies (Fig. 2b). This zonally uniform positive anomalies between middle and high latitudes denotes the development of the negative NAM. After the SSW onset date for displacement events (P3), the Arctic region is still occupied by the positive height anomalies, but the anomaly magnitude weakens and the coverage shrinks as compared with the preceding period (Fig. 2c).
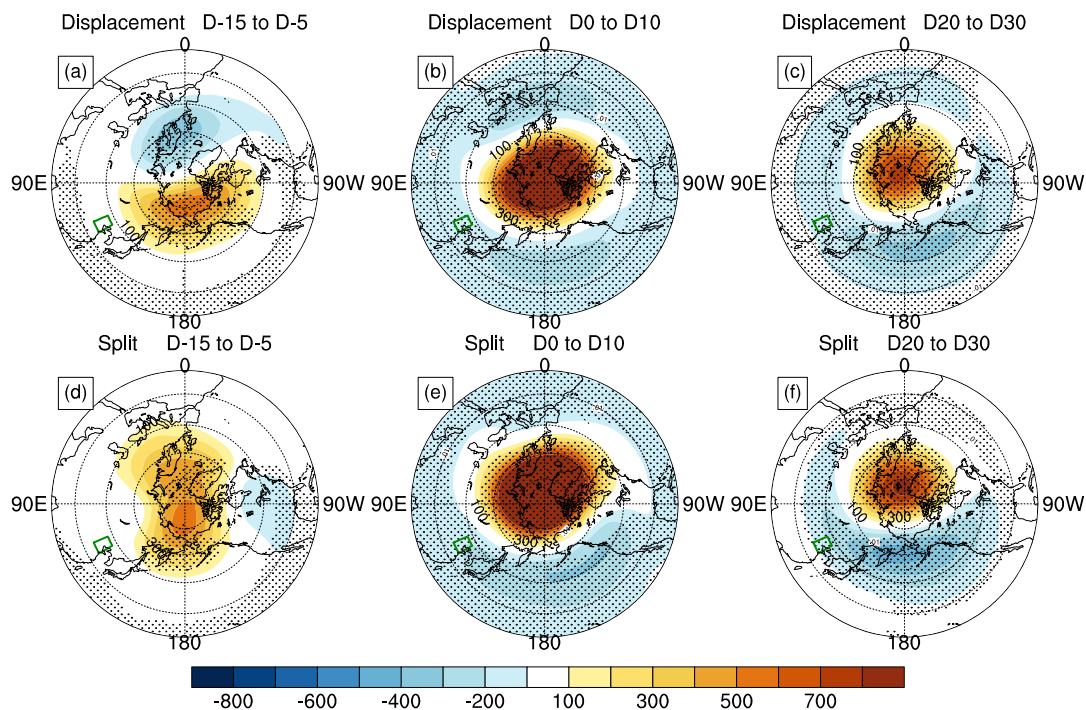
Figure 2: Composite geopotential height anomalies in the Northern Hemisphere at 10 hPa during three periods of the SSW for vortex displacement events (top row) and vortex split events (bottom row). (a, d) Day -15 to day -5 in the pre-SSW period. (b, e) Day 0 to day 10 in the SSW onset period and afterwards. (c, f) Day 20 to day 30 in the SSW decaying period. The dotted regions mark the composite geopotential height anomalies at the 95% confidence level based on the two-sided Student's *t*-test.

In the pre-SSW period for split events (P1), the polar vortex weakens as positive height anomalies occupy most of the Arctic (Fig. 2d). The positive height anomaly elongated in two directions, one toward the Nova Zembla, and the other toward the Bering Strait and the North Pacific with a narrow band crossing the North Pole covered with positive height anomalies. This elongation of the positive anomalies is probably related to the dynamical role of the wavenumber-2. Weak negative height anomalies are seen over the Great Lakes, implying the vortex is far biased from the Arctic. In the SSW onset period (P2) for events, a negative NAM-like pattern forms: similar to the circulation change for displacement SSWs, the Arctic is occupied by positive height anomalies with the maximum exceeding 800 gpm (Fig. 2e). In the SSW decaying period (P3) for split events, the negative NAM-like pattern gradually weakens (Fig. 2f).

In short, displacement and split SSW events show somewhat differences in the stratospheric circulation anomalies before the SSWs onset. The displacement SSWs is preceded by a wavenumber-1-like circulation pattern, while the split SSWs is preceded by a wavenumber-2-like circulation pattern. In the SSW onset and decaying periods for both displacement and split SSWs, a negative NAM is observed. Since the stratospheric NAM signal can propagate downward to the troposphere, which might affect the tropospheric meteorological conditions, we will examine the tropospheric evolutions.

4.2. Evolution of mid-tropospheric circulation anomalies

230   Figure 3 shows evolutions of the geopotential height anomalies at 500 hPa for displacement and split SSWs. Before the displacement SSWs onset (P1), the tropospheric height anomalies also present wavenumber 1 pattern. In the Pacific sector, the anomalous low center is located over the Aleutian Islands, and the anomalous high center is located over subtropical Pacific (Fig. 3a). The general pattern resembles the negative PNA, which amplifies the climatological wavenumber 1. The strengthening wavenumber 1 can propagate upward to disturb the stratosphere and excite a displacement SSW event. In the

235   Atlantic sector, positive height anomalies develop over the Greenland and North Atlantic. In the SSW onset period (P2) for displacement events, positive anomalies occur in the Arctic, negative height anomalies occur in northern Eurasia and northern North America at high latitudes. Meanwhile, two negative anomaly centers appear over the North Pacific, and positive height anomalies occur in western Eurasia at midlatitudes (Fig. 3b). After the displacement SSW onset (P3), large negative height anomalies appear over Nova Zembla extending westward, while positive height anomalies form in

240   Greenland and the Arctic, resembling the negative phase of the NAO (Fig. 3c). In the Pacific sector, a strong positive height anomaly center appears over the North Pacific, and negative anomalies appear over the western coasts of North America, implying the phase conversion of the PNA teleconnection from positive to negative.
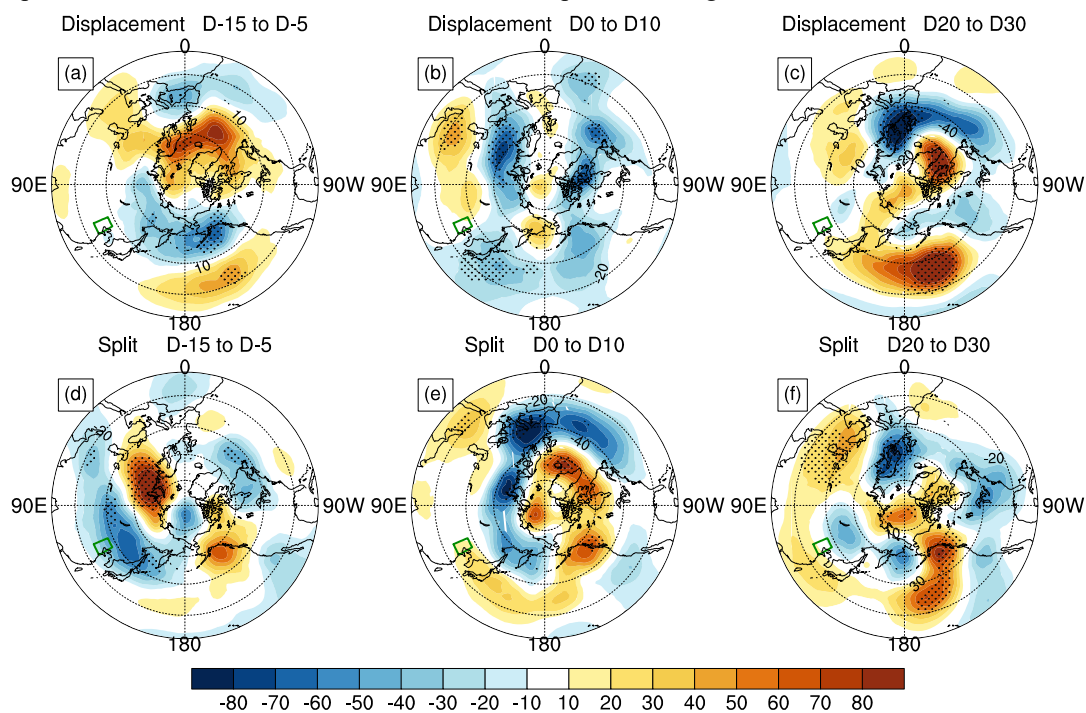
Figure 3: As in Figure 2 but for composite geopotential height anomalies in the Northern Hemisphere at 500 hPa during three
245   **periods of the SSW for vortex displacement events (top row) and vortex split events (bottom row). The dotted regions mark the composite geopotential height anomalies at the 95% confidence level based on the two-sided Student's *t*-test.**

In the pre-SSW period for split SSW (P1), the geopotential height anomalies present a wavenumber-2 pattern (Fig. 3d). Two anomalous low centers are located in eastern Siberia and eastern Canada, respectively, while two anomalous high centers are correspondingly located around the Urals and Alaska. This height anomaly pattern is in phase with and therefore amplifies the climatological wavenumber 2. The enhanced wavenumber 2 can also propagate upward into the stratosphere and split the polar vortex. In the SSW onset period (P2) for split events, positive height anomalies occur in the Arctic Canada, Greenland, Iceland, and the midlatitude Pacific, while negative height anomalies appear in northern Eurasia and the midlatitude Atlantic (Fig. 3e). In the Atlantic sector, a negative NAO-like anomaly pattern generates. In the SSW decaying period (P3) for split SSWs, the negative NAO-like anomaly pattern still persists in the Atlantic sector, while anomalous high over the Urals is stronger during this period for split (Fig. 3f) than displacement.

4.3. Evolution of the near-surface temperature anomalies

The distribution of the near surface temperature anomalies at a 2-meter height (t2m) during three periods are shown Fig. 4 for displacement SSWs and split SSWs. Before the SSW onset (P1) for displacement events, warm anomalies appear in the Arctic Canada, Greenland, and most parts in the Central and East US, whereas in the western coasts of the US, cold anomalies are evident (Fig. 4a). This temperature pattern is probably related to development of the positive PNA. Warm anomalies develop in the high latitudes of the Eurasian continent, and warm anomalies appear in parts of the southern Eurasia. The temperature anomalies in the BTH region are relatively weak. In the SSW onset period (P2), the cold anomalies in northern Eurasia at high latitudes weaken with its coverage shrank (Fig. 4b). Most parts of the Eurasian and North American continents are controlled by warm anomalies, corresponding to a dormant period of weakening east Asian monsoon. Warm anomalies in North China and weakened east Asian monsoon are consistent with the worsening atmospheric quality (shown later). After the SSW onset (P3) for displacement events, areas covered with warm anomalies further shrink, and cold anomalies are confined to the Arctic, the Bering Strait, and North America (Fig. 4c).
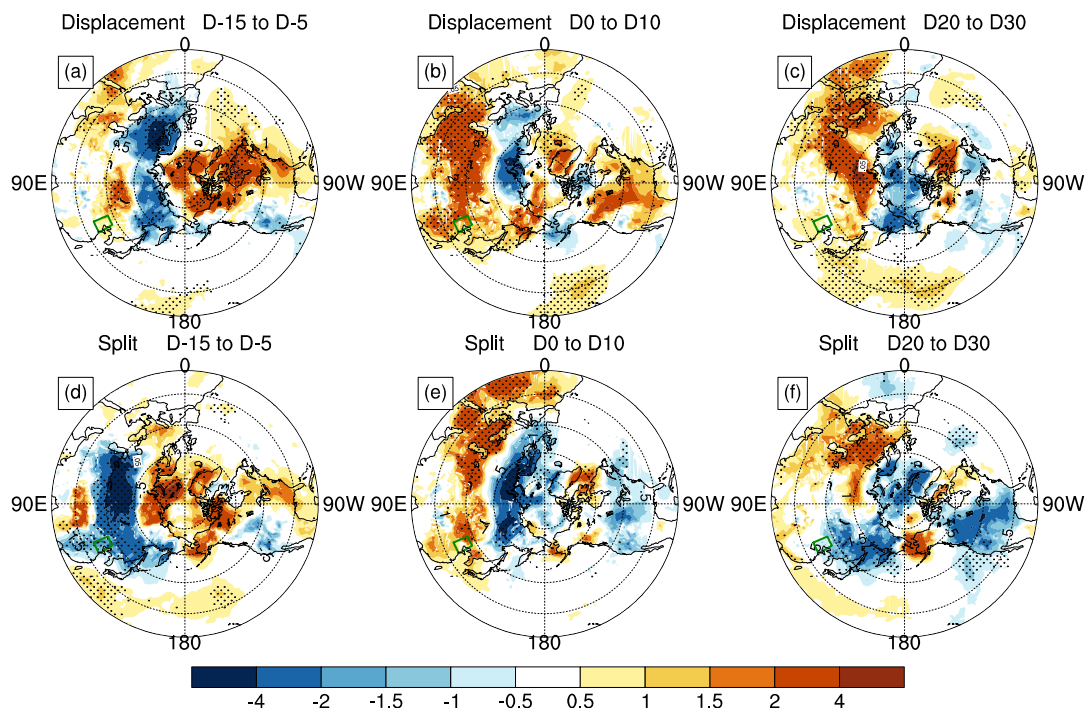
Figure 4: Composite 2-meter temperature (t2m) anomalies in the Northern Hemisphere during three periods of the SSW for
270 **vortex displacement events (top row) and vortex split events (bottom row). (a, d) Day -15 to day -5 in the pre-SSW period. (b, e)**
Day 0 to day 10 in the SSW onset period and afterwards. (c, f) Day 20 to day 30 in the SSW decaying period. The dotted regions
mark the composite t2m anomalies at the 95% confidence level based on the two-sided Student's *t*-test.

In the pre-SSW period (P1) for split events, warm anomalies are also observed over the Arctic and the eastern part of the

North American continent, while large cold anomalies appear in the Eurasian midlatitudes (Fig. 4d), implying strong cold

275 advection in North China denoted by the local cold anomalies. In contrast, the cold anomalies in the western US are much

weaker. In the onset period (P2) for split SSW events, high-latitude Eurasia and most part of North America are covered by

cold anomalies, while the mid- and low-latitudes of Eurasia are dominated by warm anomalies (Fig. 4e). Warm anomalies

and weakened east Asian winter monsoon are consistent with a period of higher air particulate concentration (shown later).

After the split SSW onset (P3), the warm anomalies in the Eurasia weaken with the coverage shrank (Fig. 8f). Meanwhile,

280 cold anomalies extend to East Asia as the cold anomalies in North America further intensify (Fig. 4f). Cold anomalies

possibly denote that the winter monsoon might enhance as the stratospheric signal propagates downward to the troposphere,

and a cleaning process of the atmospheric environment in the BTH region happens.

5. Local meteorological conditions in the BTH region

During different periods of the SSW, the stratosphere-troposphere coupling is different. In the P1 period, the tropospheric

285 waves propagate upward and begin to disturb the stratosphere. In the P2 period, the stratospheric variation reaches the

climax. In the P3 period, the stratospheric signal propagates downward to the lower troposphere and poses a potential impact on the regional environment. Previous studies have shown that the boundary layer height can suitably measure the diffusion potential for the air particulates (Huang et al., 2018, 2020). The boundary layer height (BLH) anomalies during different periods of the SSW are shown in Fig. 5 for displacement and split SSWs. By comparison, the BLH anomalies are not so

290 evident during displacement events than during split events. In the pre-SSW period for displacement events, negative PLH anomalies occur to the east of BTH region in the pre-SSW period (Fig. 5a). The negative PLH anomalies still persist in the Bohai Sea during the SSW onset period, and no simultaneous evident anomalies are found in the BTH region (Fig. 5b). Weak and insignificant positive PLH anomalies are observed during the SSW decaying periods for displacement events (Fig. 5c), which is consistent with the relatively weak downward propagation of stratospheric pulse associated with displacement

295 SSWs.

In contrast, the evolution of the PLH anomalies is more dramatic during split SSWs than during displacement SSWs. Specifically, in the pre-SSW period for split events, positive PLB anomalies are observed, which is conducive to the diffusion of air particulates (Fig. 5d). In the SSW onset period for split events, negative boundary layer height anomalies form in the BTH region, which is conducive to the accumulation of air particulates in the near surface layer (Fig. 5e). In

300 SSW decaying period for split events, the boundary layer height rises again (Fig. 5f), which is consistent with the strong downward propagation of the stratospheric anomalies for split events.
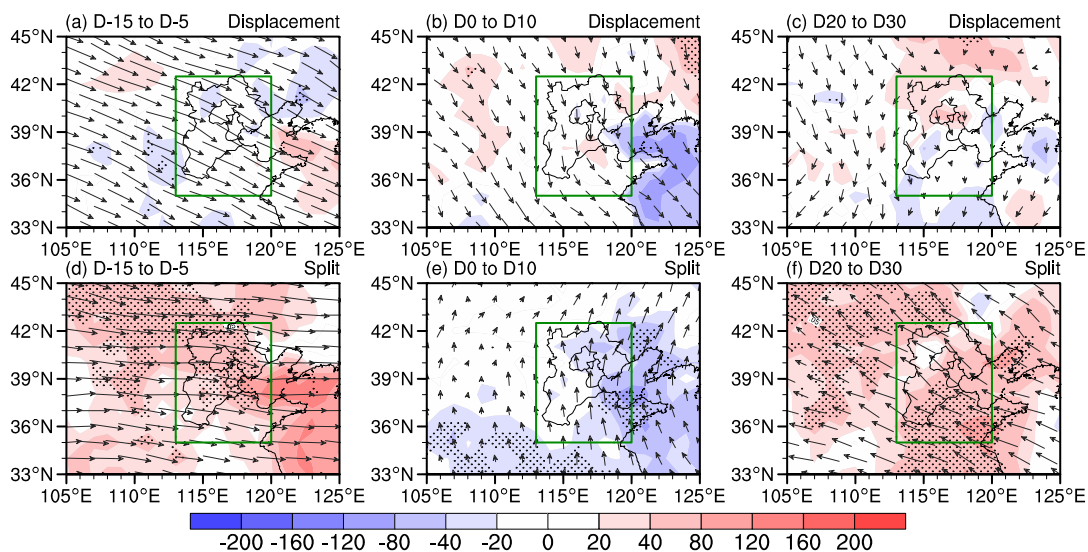
Figure 5: Composite planetary layer height (PLH; shadings) and 850-hPa wind (vector) anomalies in the BTH region during three periods of the SSW for vortex displacement events (top row) and vortex split events (bottom row). (a, d) Day -15 to day -5 in the
305 **pre-SSW period. (b, e) Day 0 to day 10 in the SSW onset period and afterwards. (c, f) Day 20 to day 30 in the SSW decaying period. The dotted regions mark the composite PLH anomalies at the 90% confidence level based on the two-sided Student's *t*-test.**

6. Atmospheric environment in BTH region during two types of SSWs

The evolutions of the stratospheric circulation and the local meteorological conditions have been analyzed during three periods for the two types of SSWs. Next, we will show the corresponding evolutions of the atmospheric environment in the BTH region.

6.1. Daily minimum visibility in the BTH region

The PM$_{2.5}$ concentration in China is not a standard observational variable before 2013, so a composite of the atmospheric environment using the air particulate concentration is unavailable (Fan et al., 2021). The daily minimum visibility is a substitute variable for the PM$_{2.5}$ concentration to measure the air quality in the BTH region, which is extracted from the historical meteorological observations. The composite evolutions of the daily minimum visibility during the displacement and split SSW events are shown in Fig. 6 for Beijing and Tianjin (note that the minimum visibility from the historical meteorological data in Hebei stations are missing in several years, and we exclude stations from Hebei). During the two types of SSW events, the minimum visibility exhibits a consistent change. The visibility during the early stage (day -20 to day -1) of the SSW is far, denoting a clean sky and pleasant atmospheric environment. During the SSW onset and afterward (day 0 to day 20), the minimum visibility decreases and the air particulate concentration might increase. In the decaying period of the SSWs (day 21 to day 40), the visibility in the cities of Beijing and Tianjin further increases again, indicating a clean atmospheric environment and an increase in the air particulates, which might be due to the downward propagation of stratospheric negative NAM signal.

Comparison between the minimum visibility change during two types of SSWs, it can also be found that changes in the minimum visibility is larger for split SSW events than for displacement SSW events. The minimum visibility of Beijing and Tianjin is 9.4 km on average before displacement SSWs, while it is ~10 km before the split SSWs. During the SSW onset and afterward, the minimum visibility in Beijing and Tianjin decreases to 8.7 km on average for displacement SSWs and 7.4 km for split SSWs. In the decaying period, the mean minimum visibility in Beijing and Tianjin is ~9.4 km, while it is ~9.1 km for split SSWs. Larger change of the minimum visibility in Beijing and Tianjin during the split SSW is consistent with the stronger intensity for split SSW events and its deeper downward influence on the troposphere.
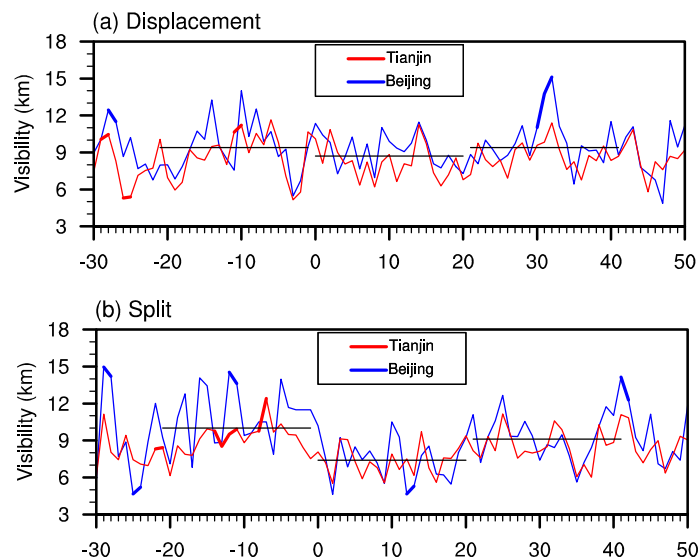
Figure 6: Composite evolution of the minimum visibility in Beijing and Tianjin during (a) polar vortex displacement SSW events and (b) polar vortex split SSW events. The blue curve denotes the time series of the minimum visibility in Beijing while the red curve denotes that in Tianjin. The thickened curves denote that the composite is significant at the 90% confidence level using the two-sided Student's *t*-test.

6.2. Haze days, fog days, and light fog days in the BTH region

Change in the minimum visibility might not be all caused by light atmospheric pollution, floating water in the air can also decrease the visibility. The composite means of the haze days, fog days and light fog days extracted from the meteorological surface observation data during the two types of SSWs are shown in Fig. 7. For both displacement and split SSWs, the number of haze days in Beijing, Tianjin and Shijiazhuang (the provincial capital of Hebei) is relatively smaller in the pre-SSW and SSW decaying periods (P1 and P3). In contrast, the haze days increases during the SSW onset period when the downward-propagating stratospheric anomalies do not reach the troposphere. Among the three cities, Shijiazhuang has the largest mean haze days during the SSWs onset stage (P2): 6 haze days for displacement SSW events and ~8 days for split SSW events. The mean haze days in Tianjin during the other two periods are less: 4–4.5 days in the P1 periods and 5.5 days in the P3 period. Tianjin has the smallest mean haze days in all periods: 0.5 days in the P1 period for both types of SSWs, 1.5–2.5 days in the P2 period, and 1–1.5 days in the P3 period. The number of haze days in Beijing falls between Tianjin and Shijiazhuang, and change trends from P1 to P2 (increasing) or from P2 to P3 (decreasing) is similar among the three cities (Fig. 7a and d).
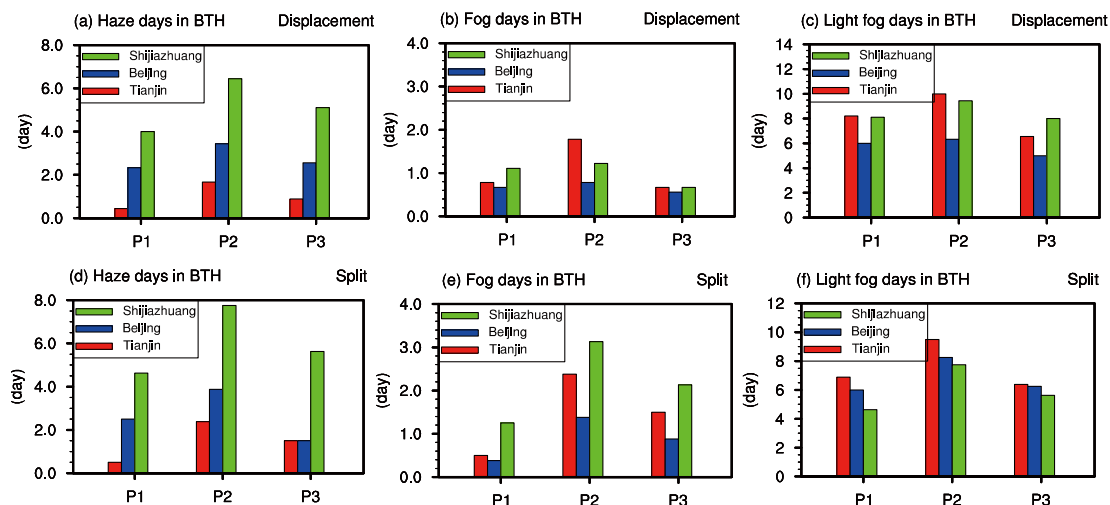
350 **Figure 7: Statistics of three environmental metrics during the three periods of displacement SSWs (top row) and split SSWs (bottom row). P1 denotes the pre-SSW period from day -20 to day -1, P2 denote the SSW onset period from day 0 to day 20, and P3 denote the SSW decaying period from day 21 to day 40. Composite means in three cities are shown for mean numbers of (a, d) haze days, (b, e) fog days (visibility < 1 km) and (c, f) light fog days (visibility < 10 km).**

The fog days show similar subsesaonal variability during the both types of SSWs (Fig. 7b, e). Specifically, the number of fog

355 days in BTH region is the largest during the SSW onset stage (P2) when the stratospheric anomalies do not propagate downward to the troposphere. The number of fog days are relatively less in the pre-SSW period and the SSW decaying period (P1 and P3) (Fig. 7b and 7e). In the pre-SSW period, the number of fog days for split SSWs and displacement SSWs in the BTH region are comparable for all three cities (0.5, 2.5, and 4 days vs 0.5, 2.5, and 4.5 days). In the onset period of displacement SSWs, the mean numbers of fog days are ~0.8, 2, and 1.2 days in Beijing, Tianjin, and Shijiazhuang,

360 respectively. In the onset period of split SSWs, the numbers of fog days are correspondingly ~1.5, 2.5, and 3 days in Beijing, Tianjin, and Shijiazhuang. In contrast, the number of fog days during the split SSW onsets in the BTH region is larger than that during the displacement SSW onsets (P2). In the SSW decaying period, the number of fog days decreases for both displacement and split events: <1 days for displacement SSWs and 1–2 days for split SSWs. The fog days in this period are also more for split SSW events than displacement SSW events in the BTH region. Similar conclusions are also applicable to

365 the number of light fog days during two different types of SSW events (Fig. 7c, f). Tianjin has the largest number of light fog days among the three cities considered, which might be owing to the fact that Tianjin is a coastal city and the water vapor is more abundant. In general, the number of light fog days in the BTH region is larger during the SSWs onset stage (P2) than other two periods (P1 and P3) (Fig. 7c and 7f).

6.3. Aerosol optical depth in the BTH region

370 Aerosol optical depth (AOD) is a variable measuring the optical property of aerosols and reflects the atmospheric turbidity. It represents the light transmittance on the vertical gas column with the section of a unit area (Mei et al., 2018). The AOD value falls between 0 and 1 and is dimensionless. Generally, high AOD value indicates an increase in the aerosol

accumulation of the atmospheric column, which leads to a reduction of atmospheric visibility. Since the PM$_{2.5}$ concentration in China has only been systematically observed in recent years since 2013, the historical AOD data remotely sensed by

375 NASA satellites might be used to verify the global air particulate concentration (Ou et al., 2022). The distribution of AOD anomalies in the BTH region is shown in Fig. 8 during vortex displacement and split SSW events. In the pre-SSW period for both displacement and split events (P1), negative AOD anomalies are observed in the BTH region (Fig. 8a and d), which corresponds to the high minimum visibility and a cleaning period of atmospheric environment. It is noticed that the most significant anomalies develop in the north, which might be related to circulation changes in higher latitudes during the

380 northern winter.

Positive AOD anomalies are observed around the SSW onset period for both displacement and split period (Fig. 8b and e) when the circulation anomalies mainly develop in the stratosphere (see Fig. 1). The positive AOD anomalies during the P2 period are larger for split SSWs than displacement SSWs with the maximum positive anomalies (0.06 vs ~0.08) in the southern part of the BTH region. The positive AOD in the BTH region and the southern neighboring areas indicates that the

385 local atmospheric quality might worsen, and the potential air pollution during split SSWs are more series than during displacement SSWs.
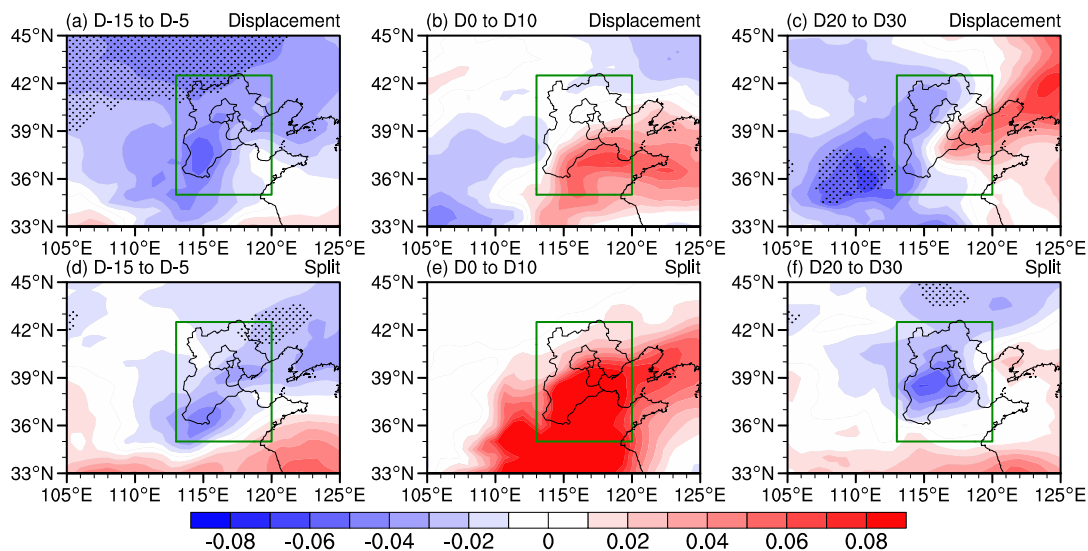
Figure 8: Composite analysis of the aerosol optical depth (AOD) anomalies in BTH the region during three periods of the SSW for vortex displacement events (top row) and vortex split events (bottom row). (a, d) Day -15 to day -5 in the pre-SSW period. (b, e)
390 **Day 0 to day 10 in the SSW onset period and afterwards. (c, f) Day 20 to day 30 in the SSW decaying period. The dotted regions mark the composite AOD anomalies at the 90% confidence level based on the two-sided Student's _t_-test.**

Negative AOD anomalies are observed again in the decaying period (P3) for both displacement and split SSWs (Fig. 8c and f). The minimum center is located differently: the negative AOD center (the minimum value: -0.06) is over the southern neighboring area in Central China for displacement SSWs, while the negative center (the minimum value: -0.04) is just

395 situated over the southern part of the Hebei province. The cleaning effect during this period (P3) is consistent with the fact that the split SSWs signal in Figure 1 has a deeper downward propagation and a stronger impact on the near surface.

7. Summary

Using the ERA5 reanalysis data, surface meteorological observation data in the BTH region, and aerosol optical depth (AOD) from the MERRA2 reanalysis, the subseasonal evolutions of air environment in the BTH region and related changes of
400 stratospheric and tropospheric circulation during displacement and split SSW events are systematically analyzed, respectively. The main conclusions are as follows.

i. Seventeen major SSW events (the marginal ones have been removed from our analysis) are identified in the Northern Hemisphere from 1981–2021, including 8 displacement SSWs and 9 split SSWs. On average, the circumpolar easterly anomalies can persist for 45 days (day -10 to day 35) for displacement SSWs, while the easterly anomalies can persist
405 for 65 days (day -15 to day 50) for split SSWs. Namely, the mean duration for split SSWs is longer than that for displacement SSWs. The stratospheric circulation anomalies associated with displacement SSWs can propagates downward to 500–200 hPa, while the stratospheric signals for split SSWs can propagate further downward to below 500 hPa or even to the near surface. In other words, the split SSW events change more violently, and the stratospheric signal propagation is overall more evident.

410 ii. As measurements for the atmospheric environment and air quality, the minimum visibility, haze days, fog days, light fog days, and aerosol optical depth (AOD) in the BTH region show consistent subseasonal changes during both displacement and split SSWs. Specifically, the atmosphere in the pre-SSW period is clean with far visibility and fewer haze and fog days. In the SSW onset period when the stratospheric circulation anomalies do not propagate downward to the near surface, the air quality seems to worsen with less remote visibility and more haze and fog days. In the SSW
415 decaying period when the stratospheric disturbance signal has reached the lower troposphere, the air quality in the BTH area improves with far visibility, and fewer haze and fog days again. By comparison, the subseasonal variation of the atmospheric environment in the BTH region is more evident and robust during split SSWs events than displacement SSWs, which is consistent with the stronger change in the circulation, longer duration, and further downward propagation of the stratospheric signals for the former than the latter.

420 iii. In the pre-SSW periods for both displacement and split SSW events, some differences are also noticeable. The displacement SSW events are dominated by the wavenumber 1 anomaly pattern from the troposphere to the stratosphere, while the split SSW events are dominated by the wavenumber 2 anomaly pattern. The enhanced east Asian monsoon is more significant during the pre-SSW period for split events than for displacement events. In the SSW onset period, the winter monsoon weakens for both displacement and split SSWs, although the circulation
425 anomalies are larger for split SSWs than displacement SSWs. In the SSW decaying period, larger cold anomalies develop in east Asia for split SSWs than displacement SSWs, possibly due to the further downward propagation of the

stratospheric disturbance signals for the former than the latter. It is also observed that the cold anomalies appear in North America after the SSW onset for both displacement and split events (Cao et al., 2019; Rao et al., 2021), and the cold anomalies in North America are also larger for split SSWs than displacement SSWs.

430 iv. With the gradual evolution of the large-scale circulation from the stratosphere to the troposphere during the SSW events, the boundary layer conditions in the BTH region have also changed accordingly. The boundary layer height in the BTH region shows positive, negative, and then positive anomalies from the pre-SSW period, to the SSW onset period, and then to the SSW decaying period, respectively. Change in the local meteorological conditions are also consistent with the subseasonal variation of the local air quality in the BTH region. In contrast, the variation of the

435 boundary layer height during displacement SSWs do not necessarily cooperate with the large-scale circulation from the stratosphere to the troposphere to modulate the atmospheric environment in the BTH region. It can be inferred that the stratospheric pulse signal with further downward propagation might affect the local meteorological conditions for particulate diffusion and dilution.

With China's strict implementation of energy conservation and emission reduction policies in the past 10 years, the air

440 quality and atmospheric environment have improved significantly (Ding et al., 2019). Compared with the some previous studies emphasizing the possible impact of tropospheric meteorological conditions and teleconnections on the air quality in the BTH region (Yin and Wang, 2017; Huang et al., 2018; Zhai et al., 2019), our study further points out some typical stratospheric disturbance such as SSWs can also modulate the subseasonal variability of the air quality in one of the most populated regions across China. Considering that the stratospheric circulation anomalies can lead the tropospheric circulation

445 anomalies by days to weeks, an improved predictive skill might become possible after the stratospheric signals are also considered in the subseasonal atmospheric environment forecast systems. With abundant SSW samples, our study has also confirmed the generalization of the results based on individual case studies (Lu et al., 2021a, 2022). The possible impact of the stratospheric disturbance on the air quality in other subregions across China is still not well understood, deserving further investigation in the future.

450 **Acknowledgements**

This work was supported by the National Natural Science Foundation of China (Grant Nos. 42088101 and 42175069), and the National Key R&D Program of China (2018YFC1505602).

Data Availability Statement

The ECMWF provides the ERA5 reanalysis (https://cds.climate.copernicus.eu/). The NASA provides the MERRA2

455 atmospheric reanalysis (https://disc.gsfc.nasa.gov/datasets). The daily observation data is from the China Meteorological Information Center (http://data.cma.cn/).

References

Baldwin, M. P. and Dunkerton, T. J.: Propagation of the Arctic Oscillation from the stratosphere to the troposphere, J. Geophys. Res., 104, 30937–30946, https://doi.org/10.1029/1999JD900445, 1999.

460 Baldwin, M. P. and Dunkerton, T. J.: Stratospheric harbingers of anomalous weather regimes, Science, 294, 581–584, https://doi.org/10.1126/science.1063315, 2001.

Baldwin, M. P., Ayarzagüena, B., Birner, T., Butchart, N., Butler, A. H., Charlton-Perez, A. J., Domeisen, D. I. V., Garfinkel, C. I., Garny, H., Gerber, E. P., Hegglin, M. I., Langematz, U., and Pedatella, N. M.: Sudden stratospheric warmings, Rev. Geophys., 59, e2020RG000708, https://doi.org/10.1029/2020rg000708, 2021.

465 Bu, X., Xie, Z., Liu, J., Wei, L., Wang, X., Chen, M., and Ren, H.: Global PM2.5-attributable health burden from 1990 to 2017: Estimates from the global burden of disease study 2017, Environ. Res., 197, 111123, https://doi.org/10.1016/j.envres.2021.111123, 2021.

Butler, A. H., Seidel, D. J., Hardiman, S. C., Butchart, N., Birner, T., and Match, A.: Defining sudden stratospheric warmings, Bull. Am. Meteor. Soc. 96, 1913–1928, https://doi.org/10.1175/BAMS-D-13-00173.1, 2015.

470 Butler, A. H., Lawrence, Z. D., Lee, S. H., Lillo, S. P., and Long, C. S.: Differences between the 2018 and 2019 stratospheric polar vortex split events, Quarterly Q. J. Roy. Meteor. Soc., 146, 3503–3521, https://doi.org/10.1002/qj.3858, 2020.

Cao, C., Chen, Y., Rao, J., Liu, S., Li, S., and Ma, M.: Statistical characteristics of major sudden stratospheric warming events in CESM1-WACCM: A comparison with the JRA55 and NCEP/NCAR reanalyses, Atmosphere, 10, 519, 2019.

Chang, L., Wu, Z., and Xu, J.: A comparison of haze pollution variability in China using haze indices based on observations,
475 Sci. Tot. Environ., 715, 136929, https://doi.org/10.1016/j.scitotenv.2020.136929, 2020.

Charlton, A. J. and Polvani, L. M.: A new look at stratospheric sudden warmings. part i: climatology and modeling benchmarks, J. Clim., 20, 449–469, https://doi.org/10.1215/S0012-7094-69-03643-6, 2007.

Chen, L., Zhu, J., Liao, H., Yang, Y., and Yue, X.: Meteorological influences on PM2.5 and O3 trends and associated health burden since China's clean air actions, Sci. Tot. Environ., 744, 140837, https://doi.org/10.1016/j.scitotenv.2020.140837,
480 2020.

Dang, R. and Liao, H.: Severe winter haze days in the Beijing-Tianjin-Hebei region from 1985 to 2017 and the roles of anthropogenic emissions and meteorology, Atmos. Chem. Phys., 19, 10801–10816, https://doi.org/10.5194/acp-19-10801-2019, 2019.

De La Cámara, A., Birner, T., and Albers, J. R.: Are sudden stratospheric warmings preceded by anomalous tropospheric
485 wave activity? J. Clim., 32, 7173–7189, https://doi.org/10.1175/JCLI-D-19-0269.1, 2019.

Ding, A., Huang, X., Nie, W., Chi, X., Xu, Z., Zheng, L., Xu, Z., Xie, Y., Qi, X., Shen, Y., Sun, P., Wang, J., Wang, L., Sun, J., Yang, X. Q., Qin, W., Zhang, X., Cheng, W., Liu, W., Pan, L., and Fu, C.: Significant reduction of PM2.5 in eastern China due to regional-scale emission control: Evidence from SORPES in 2011-2018, Atmos. Chem. Phys., 19, 11791–11801, https://doi.org/10.5194/acp-19-11791-2019, 2019.

490   Fan, H., Zhao, C., Yang, Y., and Yang, X.: Spatio-temporal variations of the PM2.5/PM10 ratios and its application to air
         pollution type classification in China, Front. Environ. Sci., 9, 692440, https://doi.org/10.3389/fenvs.2021.692440, 2021.

Feng, J., Quan, J., Liao, H., Li, Y., and Zhao, X.: An air stagnation index to qualify extreme haze events in northern China, J.
         Atmos. Sci., 75, 3489–3505, https://doi.org/10.1175/JAS-D-17-0354.1, 2018.

Gelaro, R., McCarty, W., Suárez, M. J., Todling, R., Molod, A., Takacs, L., Randles, C. A., Darmenov, A., Bosilovich, M.
495   G., Reichle, R., Wargan, K., Coy, L., Cullather, R., Draper, C., Akella, S., Buchard, V., Conaty, A., da Silva, A. M., Gu,
         W., Kim, G. K., Koster, R., Lucchesi, R., Merkova, D., Nielsen, J. E., Partyka, G., Pawson, S., Putman, W., Rienecker,
         M., Schubert, S. D., Sienkiewicz, M., and Zhao, B.: The modern-era retrospective analysis for research and applications,
         version 2 (MERRA-2), J. Clim., 30, 5419–5454, https://doi.org/10.1175/JCLI-D-16-0758.1, 2017.

Hersbach, H., Bell, B., Berrisford, P., Hirahara, S., Horányi, A., Muñoz-Sabater, J., Nicolas, J., Peubey, C., Radu, R.,
500   Schepers, D., Simmons, A., Soci, C., Abdalla, S., Abellan, X., Balsamo, G., Bechtold, P., Biavati, G., Bidlot, J.,
         Bonavita, M., De Chiara, G., Dahlgren, P., Dee, D., Diamantakis, M., Dragani, R., Flemming, J., Forbes, R., Fuentes,
         M., Geer, A., Haimberger, L., Healy, S., Hogan, R. J., Hólm, E., Janisková, M., Keeley, S., Laloyaux, P., Lopez, P.,
         Lupu, C., Radnoti, G., de Rosnay, P., Rozum, I., Vamborg, F., Villaume, S., and Thépaut, J. N.: The ERA5 global
         reanalysis, Quarterly Q. J. Roy. Meteor. Soc., 146, 1999–2049, https://doi.org/10.1002/qj.3803, 2020.

505   Hu, B., Chen, R., Xu, J., Yang, G., Xu, D., Chen, C., and Zhao, Y.: Health effects of ambient ultrafine (nano) particles in
         haze, Chin. Sci. Bull., 60, 2808–2823, https://doi.org/10.1360/N972014-01404, 2015.

Hu, J., Ren, R., and Xu, H.: Occurrence of winter stratospheric sudden warming events and the seasonal timing of spring
         stratospheric final warming, J. Atmos. Sci., 71, 2319–2334, https://doi.org/10.1175/JAS-D-13-0349.1, 2014.

Huang, R. J., Zhang, Y., Bozzetti, C., Ho, K. F., Cao, J. J., Han, Y., Daellenbach, K. R., Slowik, J. G., Platt, S. M., Canonaco,
510   F., Zotter, P., Wolf, R., Pieber, S. M., Bruns, E. A., Crippa, M., Ciarelli, G., Piazzalunga, A., Schwikowski, M.,
         Abbaszade, G., Schnelle-Kreis, J., Zimmermann, R., An, Z., Szidat, S., Baltensperger, U., El Haddad, I., and Prévôt, A.
         S. H.: High secondary aerosol contribution to particulate pollution during haze events in China, Nature, 514, 218–222,
         https://doi.org/10.1038/nature13774, 2015.

Huang, W., Yu, Y., Yin, Z., Chen, H., and Gao, M.: Appreciable role of stratospheric polar vortex in the abnormal diffusion
515   of air pollutant in North China in 2015/2016 winter and implications for prediction, Atmos. Environ., 259, 118549,
         https://doi.org/10.1016/j.atmosenv.2021.118549, 2021.

Huang, X., Wang, Z., and Ding, A.: Impact of aerosol-PBL interaction on haze pollution: multiyear observational evidences
         in North China, Geophys. Res. Lett., 45, 8596–8603, https://doi.org/10.1029/2018GL079239, 2018.

Huang, X., Ding, A., Wang, Z., Ding, K., Gao, J., Chai, F., and Fu, C.: Amplified transboundary transport of haze by
520   aerosol–boundary layer interaction in China, Nature Geoscience, 13, 428–434, https://doi.org/10.1038/s41561-020-
         0583-4, 2020.

Karpechko, A. Y., Charlton-Perez, A., Balmaseda, M., Tyrrell, N., and Vitart, F.: Predicting Sudden Stratospheric Warming 2018 and its climate impacts with a multimodel ensemble, Geophys. Res. Lett., 45, 13538–13546, https://doi.org/10.1029/2018GL081091, 2018.

525 Li, J., Liao, H., Hu, J., and Li, N.: Severe particulate pollution days in China during 2013–2018 and the associated typical weather patterns in Beijing-Tianjin-Hebei and the Yangtze River Delta regions, Environmental Pollution, 248, 74–81, https://doi.org/10.1016/j.envpol.2019.01.124, 2019.

Li, K., Liao, H., Cai, W., and Yang, Y.: Attribution of anthropogenic influence on atmospheric patterns conducive to recent most severe haze over eastern China, Geophys. Res. Lett., 45, 2072–2081, https://doi.org/10.1002/2017GL076570, 530 2018.

Li, Z., Lau, W. K. M., Ramanathan, V., Wu, G., Ding, Y., Manoj, M. G., Liu, J., Qian, Y., Li, J., Zhou, T., Fan, J., Rosenfeld, D., Ming, Y., Wang, Y., Huang, J., Wang, B., Xu, X., Lee, S. S., Cribb, M., Zhang, F., Yang, X., Zhao, C., Takemura, T., Wang, K., Xia, X., Yin, Y., Zhang, H., Guo, J., Zhai, P. M., Sugimoto, N., Babu, S. S., and Brasseur, G. P.: Aerosol and monsoon climate interactions over Asia, Rev. Geophys., 54, 866–929, https://doi.org/10.1002/2015RG000500, 535 2016.

Liu, S. M., Chen, Y. H., Rao, J., Cao, C., Li, S. Y., Ma, M. H., and Wang, Y. Bin: Parallel comparison of major sudden stratospheric warming events in CESM1-WACCM and CESM2-WACCM, Atmosphere, 10, 679, https://doi.org/10.3390/atmos10110679, 2019.

Lu, Q., Rao, J., Guo, D., Yu, M., and Yu, Y.: Downward propagation of sudden stratospheric warming signals and the local 540 environment in the Beijing-Tianjin-Hebei region: A comparative study of the 2018 and 2019 winter cases, Atmos. Res., 254, 105514, https://doi.org/10.1016/j.atmosres.2021.105514, 2021a.

Lu, Q., Rao, J., Liang, Z., Guo, D., Luo, J., Liu, S., Wang, C., and Wang, T.: The sudden stratospheric warming in January 2021b, Environ. Res. Lett., 16, 084029, https://doi.org/10.1088/1748-9326/ac12f4, 2021b.

Lu, Q., Rao, J., Shi, C., Guo, D., Wang, J., Liang, Z., and Wang, T.: Observational subseasonal variability of the PM2.5 545 concentration in the Beijing-Tianjin-Hebei area during the January 2021 sudden stratospheric warming, Adv. Atmos. Sci., 1–44, https://doi.og/10.1007/s00376-022-1393-y, 2022.

Matthewman, N. J., Esler, J. G., Charlton-Perez, A. J., and Polvani, L. M.: A new look at stratospheric sudden warmings. Part III: Polar vortex evolution and vertical structure, J. Clim., 22, 1566–1585, https://doi.org/10.1175/2008JCLI2365.1, 2009.

550 Mei, L., Rozanov, V., Vountas, M., Burrows, J. P., and Richter, A.: XBAER-derived aerosol optical thickness from OLCI/Sentinel-3 observation, Atmos. Chem. Phys., 18, 2511–2523, https://doi.org/10.5194/acp-18-2511-2018, 2018.

Mitchell, D. M., Charlton-Perez, A. J., and Gray, L. J.: Characterizing the variability and extremes of the stratospheric polar vortices using 2D moment analysis, J. Atmos. Sci., 68, 1194–1213, https://doi.org/10.1175/2010JAS3555.1, 2011.

Ou, Y., Li, Z., Chen, C., Zhang, Y., Li, K., Shi, Z., Dong, J., Xu, H., Peng, Z., Xie, Y., and Luo, J.: Evaluation of MERRA2
555   aerosol optical and component properties over China using SONET and PARASOL/GRASP data, Remote Sens., 14, https://doi.org/10.3390/rs14040821, 2022.

Rao, J. and Garfinkel, C. I.: CMIP5/6 models project little change in the statistical characteristics of sudden stratospheric warmings in the 21st century, Environ. Res. Lett., 16, 034024, https://doi.org/10.1088/1748-9326/abd4fe, 2020.

Rao, J., Ren, R., Chen, H., Yu, Y., and Zhou, Y.: The stratospheric sudden warming event in February 2018 and its
560   prediction by a climate system model, J. Geophys. Res. Atmos., 123, 13332–13345, https://doi.org/10.1029/2018JD028908, 2018.

Rao, J., Ren, R., Chen, H., Liu, X., Yu, Y., Hu, J., and Zhou, Y.: Predictability of stratospheric sudden warmings in the Beijing climate center forecast system with statistical error corrections, J. Geophys. Res. Atmos., 124, 8385–8400, https://doi.org/10.1029/2019JD030900, 2019a.

565 Rao, J., Garfinkel, C. I., Chen, H., and White, I. P.: The 2019 new year stratospheric sudden warming and its real-time predictions in multiple S2S models, J. Geophys. Res. Atmos., 124, 11155–11174, https://doi.org/10.1029/2019JD030826, 2019b.

Rao, J., Garfinkel, C. I., and White, I. P.: Predicting the downward and surface influence of the February 2018 and January 2019 sudden stratospheric warming events in subseasonal to seasonal (S2S) models, J. Geophys. Res. Atmos., 125,
570   e2019JD031919, https://doi.org/10.1029/2019JD031919, 2020.

Rao, J., Liu, S., and Chen, Y.: Northern Hemisphere sudden stratospheric warming and its downward impact in four Chinese CMIP6 models, Adv. Atmos. Sci., 38, 187–202, https://doi.org/10.1007/s00376-020-0250-0, 2021.

Seviour, W. J. M., Gray, L. J., and Mitchell, D. M.: Stratospheric polar vortex splits and displacements in the high-top CMIP5 climate models, J. Geophys. Res. Atmos., 121, 1400–1413, https://doi.org/10.1002/2015JD024178, 2016.

575 Wang, H. J. and Chen, H. P.: Understanding the recent trend of haze pollution in eastern China: Roles of climate change, Atmos. Chem. Phys., 16, 4205–4211, https://doi.org/10.5194/acp-16-4205-2016, 2016.

Wu, P., Ding, Y., and Liu, Y.: Atmospheric circulation and dynamic mechanism for persistent haze events in the Beijing–Tianjin–Hebei region, Adv. Atmos. Sci., 34, 429–440, https://doi.org/10.1007/s00376-016-6158-z, 2017.

Yang, Y., Liao, H., and Lou, S.: Increase in winter haze over eastern China in recent decades: Roles of variations in
580   meteorological parameters and anthropogenic emissions, J. Geophys. Res. Atmos., 121, 13050–13065, https://doi.org/10.1002/2016JD025136, 2016.

Yin, Z. and Wang, H.: Role of atmospheric circulations in haze pollution in December 2016, Atmos. Chem. Phys., 17, 11673–11681, https://doi.org/10.5194/acp-17-11673-2017, 2017.

Yin, Z., Wang, H., and Yuan, D.: Interdecadal increase of haze in winter over North China and the Huang-huai Area and the
585   weakening of the East Asia Winter Monsoon, Chin. Sci. Bull., 60, 1395–1400, https://doi.org/10.1360/N972014-01348, 2015.

Yin, Z., Wang, H., and Chen, H.: Understanding severe winter haze events in the North China Plain in 2014: Roles of climate anomalies, Atmos. Chem. Phys., 17, 1641–1651, https://doi.org/10.5194/acp-17-1641-2017, 2017.

Yu, Y., Ren, R., and Cai, M.: Dynamic linkage between cold air outbreaks and intensity variations of the meridional mass circulation, J. Atmos. Sci., 72, 3214–3232, https://doi.org/10.1175/JAS-D-14-0390.1, 2015.

Zhai, S., Jacob, D. J., Wang, X., Shen, L., Li, K., Zhang, Y., Gui, K., Zhao, T., and Liao, H.: Fine particulate matter (PM$_{2.5}$) trends in China, 2013–2018: separating contributions from anthropogenic emissions and meteorology, Atmos. Chem. Phys., 19, 11031–11041, https://doi.org/10.5194/acp-19-11031-2019, 2019.

Zhao, C., Wang, Y., Shi, X., Zhang, D., Wang, C., Jiang, J. H., Zhang, Q., and Fan, H.: Estimating the contribution of local primary emissions to particulate pollution using high-density station observations, J. Geophys. Res. Atmos., 124, 1648–1661, https://doi.org/10.1029/2018JD028888, 2019.